

Study of eclipses for Redback pulsar J1227–4853

Sanjay Kudale¹, Jayanta Roy¹, Bhaswati Bhattacharyya¹, Ben Stappers², Jayaram Chengalur¹

ABSTRACT

We present a multi-frequency study of eclipse properties of a transitional redback millisecond pulsar J1227–4853 discovered in 2014 with the GMRT. Emission from this pulsar is eclipsed at 607 MHz for about 37% of its orbit around the superior conjunction. We observe eclipse ingress and egress transition which last 12% and 15% of its orbit respectively, resulting in only 36% of the orbit being unaffected by eclipsing material. We report an excess dispersion measure (DM) at eclipse boundaries of $0.079(3)$ pc cm⁻³ and the corresponding electron column density (N_e) is $24.4(8) \times 10^{16}$ cm⁻². Simultaneous timing and imaging studies suggests that the eclipses in J1227–4853 are not caused by temporal smearing due to excess dispersion and scattering but could be caused by removal of pulsar flux due to cyclotron absorption of the pulsed signal by intra-binary material constraining the companion’s magnetic field. Additionally, near inferior conjunction at orbital phase 0.71 and 0.82 the pulsed emission is significantly delayed which is associated with a fading of the pulsed and continuum flux densities. At orbital phase ~ 0.82 , we measure a change in DM of $0.035(3)$ pc cm⁻³ and N_e of $10.8(8) \times 10^{16}$ cm⁻² associated with a dimming of up to $\sim 30\%$ of the peak flux density. Such flux fading around a fixed orbital phase is not reported for other eclipsing binaries. Moreover, this event around inferior conjunction could be caused by absorption of pulsed signal by fragmented blobs of plasma generated from mass loss through the L2 Lagrangian point.

1. Introduction

Millisecond pulsars (MSPs) are believed to be generated in a re-cycling process where the pulsar accretes mass from its companion star in a close binary system resulting in a faster

¹National Centre for Radio Astrophysics, Tata Institute of Fundamental Research, Pune 411 007, India

²Jodrell Bank Centre for Astrophysics, School of Physics and Astronomy, The University of Manchester, Manchester M13 9PL, UK

spin period via transfer of angular momentum (e.g. Bhattacharya et al. (1992)). A special class of fast spinning MSPs (spin period < 8 ms) in evolving compact binaries (less than a day), where the pulsar is in active interaction with its companion are classified as black widow and redback MSP systems. Such compact systems where companions are ablated away by energetic pulsar winds, are in general referred to as spider MSPs. In the majority of such system, the inclination of the binaries allow the intra-binary material to obscure the pulsar emission for a part of its orbit resulting in the observed eclipses. The volume occupied by the eclipsing material is well outside the companions Roche lobe, and thus is not gravitationally bound to the companion. The energy of an isotropic pulsar wind at the distance of the companion is given by \dot{E}/a^2 , where \dot{E} is the spin-down energy of the pulsar and a is the distance to the companion. \dot{E}/a^2 in redback and black widow pulsars are $\sim 10^{34}$ $erg/s/R_{\odot}^2$, whereas \dot{E}/a^2 for canonical MSPs is around $10^{29} - 10^{30}$ $erg/s/R_{\odot}^2$. Roy et al. (2015) reported the discovery of a 1.69 millisecond pulsar J1227–4853, at a dispersion measure (DM) of 43.4 pc cm $^{-3}$ associated with LMXB XSS J12270–4859, using the GMRT at 607 MHz. PSR J1227–4853 is in a 6.9 hours orbit with a companion of mass 0.17–0.46 M_{\odot} and is eclipsed for large fraction of its orbit at 607 MHz.

The majority of black widow and redback pulsars exhibit long eclipses ($>10\%$ of the orbital period) near their companion’s superior conjunctions. Thompson et al. (1994) gives a detailed prescription for investigation of the eclipse mechanism in such systems. However, the detailed study of the eclipse properties have been performed for only a few of the spider pulsars: PSR J1544+4937 (Bhattacharyya et al. 2013), PSR B1744-24A (Lyne et al. (1990), Nice & Thorsett (1992), Bilous et al. (2019)), PSR J1810+1744 (Polzin et al. 2018), PSR J1816+4510 (Polzin et al. 2020), B1957+20 (Fruchter et al. (1988), Ryba et al. (1991), Main et al. (2018), Li et al. (2019)), J2051–0827 (Stappers et al. (1996), Polzin et al. (2020)). This could be due to lack of availability of sensitive instruments operating at low frequencies, where the effects of eclipses are expected to be larger. This is addressed by some of the more recent studies (e.g. Main et al. (2018), Li et al. (2019), Polzin et al. (2018) and Polzin et al. (2020)) with sensitive observations using the Arecibo, LOFAR, upgraded GMRT (uGMRT) and the Parkes telescope.

In this paper we present a detailed study of the eclipses in the PSR J1227–4853 system at multiple frequencies. Section 2 details the observations and analysis procedure. Different sub-sections of Section 3 presents the results from study of the eclipse properties of PSR J1227–4853. Section 3.1 concentrates on main eclipses at 607 MHz. Investigation of frequency dependent eclipsing is presented in Section 3.2. In addition to the main eclipse, we also observe excess dispersion around inferior conjunction, which is reported in Section 3.3. Flux fading observed at eclipse ingress and around inferior conjunction is reported in Section 3.4. Discussions on these results and a summary are presented in Section 4.

2. Observation and analysis

Following the discovery, PSR J1227–4853 is being regularly observed using the GMRT coherent array at 607 MHz. Most of the observations reported in this paper were carried out with the legacy GMRT system using GMRT Software Back-end (GSB; Roy et al. (2010)). We generated filter-bank data products having 512×0.0651 MHz channels at $61.44 \mu\text{s}$ time resolution. These data were incoherently de-dispersed at the pulsar DM and folded with the ephemeris using PRESTO (Ransom et al. 2002). We used a multi-Gaussian template for extracting times-of-arrival (TOAs) at each observing epoch. The TOAs were generated with typically ~ 4 minutes integration time for achieving optimal signal-to-noise (S/N) as well as a time resolution sufficient to probe eclipse transition. Similar time resolution was used in the imaging analysis (described below). PSR J1227–4853 is eclipsed for around 2.8 hours, which is $\sim 40\%$ of its orbit (Roy et al. 2015). Many of the timing observations typically of ~ 1 hour duration regularly performed with the GMRT, partially samples eclipse phase allowing us to probe eclipse characteristics of PSR J1227–4853.

In order to probe the frequency dependence of eclipse characteristics we observed PSR J1227–4853 simultaneously at 300–500 and 550–750 MHz using the upgraded GMRT (uGMRT; Gupta et al. 2018). The increase of instantaneous band-width compensates for the reduction of the coherent array gain compared to our earlier observations resulting from splitting antennas into two sub-arrays. The 550–750 MHz data was recorded in 4096×0.0488 MHz filter-bank output at $81.92 \mu\text{s}$ time resolution, which was incoherently de-dispersed and folded. Whereas 300–500 MHz data was recorded in 512×0.390 MHz coherently de-dispersed filter-bank format at $10.24 \mu\text{s}$ time resolution in order to avoid residual dispersion smearing reducing the TOA uncertainties.

Visibility data were recorded with ~ 2 seconds time resolution in parallel with the beam-formed data. Every observation of the target pulsar is accompanied with observation of the phase calibrator 1154–350 which is sufficiently close and strong enough to perform bandpass and gain calibration (7.8 Jy). Continuum imaging analysis is carried using an automated imaging pipeline (Kudale, Chengalur, Mohan, in preparation) which is composed of *flagcal* (Chengalur 2013), *PyBDSM* (Mohan et al. 2015) & *CASA*³. In total three self calibration and imaging cycles are carried out, of which the first two cycles of gain calibration were done with phase-only calibration and last was done with amplitude and phase calibration. Final imaging after the last self-calibration cycle is done only for the duration for which pulsar was in the non-eclipsing phase of its orbit. This enabled us to estimate average flux density on given observation epoch. The self-calibrated uvdata were then used to generate snapshot

³<http://www.casa.nrao.edu>

images of the pulsar with an average time duration ~ 3 minutes to generate the lightcurve. Since the pulsar is a point source, we use the peak flux density obtained by fitting a 2D Gaussian to the pulsar image to estimate pulsar flux density. This was done using the *imfit* task of CASA, with same region box around the pulsar used to do the fit in all image frames. To obtain errorbars on the flux densities we used the task *imstat* of CASA to estimate the rms near the pulsar location. This we feel, is a conservative, but better estimate of the true uncertainty than the formal error to the peak of the Gaussian fit.

3. Results

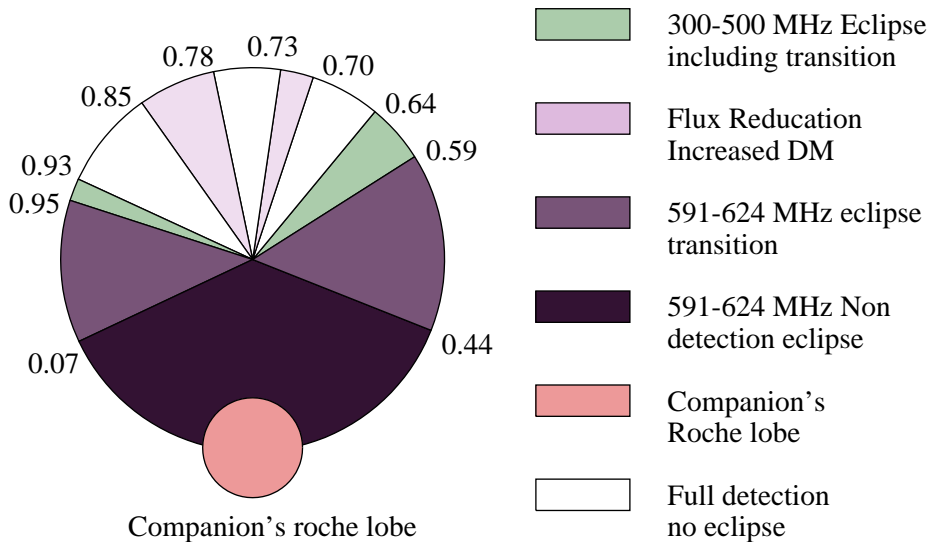


Fig. 1.— Top view of companion’s Roche lobe and geometry of eclipsing binary. Companion’s Roche lobe and orbit are approximately to the scale assuming the radio timing model (Roy et al. 2015).

Even though the orbital period of PSR J1227–4853 is ~ 6.9 hours, the source is visible at the GMRT sky for only ~ 3.5 hours. Each observing session, typically of 1 hour duration, covers only a part of the orbital phase. However, regular timing observations performed with

the GMRT, allowed us to use this collection of observations to probe eclipse boundaries. Similar to Fig. 1 by Polzin et al. (2019), we show a schematic diagram of the companion’s orbit for PSR J1227–4853 system highlighting companion’s Roche lobe ($R_L = 0.51 R_\odot$, Eggleton (1983), using $1.4 M_\odot$ as pulsar mass and $0.2 M_\odot$ as companion mass), eclipse regions at 591–624 MHz and 300–500 MHz. The observed flux fading near inferior conjunction associated with increase of the line-of-sight DM is also indicated in this figure. We describe the main results from multi frequency investigation of PSR J1227–4853 in the following sections.

3.1. Study of eclipses at 591–624 MHz

Our sample consists of 13 epochs of observations at 591–624 MHz, out of which 6 observations include an eclipse ingress and 7 observations include an eclipse egress. Timing residuals of these observations are presented in Fig. 2. We observed substantial delays in the timing residuals ($888(28) \mu\text{s}$) due to line-of-sight excess DMs at the eclipse boundaries associated with corresponding drops in the flux density. Moreover, we find that the eclipse ingress and egress transitions are spread over a range of orbital phases as shown by shaded regions in Fig. 2. The eclipse ingress transition starts from $\phi_B = 0.95$ and ends at 0.07, resulting in total ingress duration of 0.12 in orbital phase. Using the detection at latest ingress phase ($\phi_B \sim 0.07$) and earliest egress phase ($\phi_B \sim 0.44$) from a sample of 13 eclipses, we estimate the duration of the completely eclipsed phase to be 37% of the orbital period. This duration is smaller than the value reported in Roy et al. (2015), which was based on a single ingress and egress detection. The egress transition region is spread over orbital range from 0.44 to 0.59 resulting in total egress side transition duration of 0.15 in orbital phase. Thus the egress transition is seen for longer duration compared to the ingress transition (by 12.4 ± 3 minutes), which is also seen in other eclipsing binary systems, e.g. PSR J1810+1744 (Polzin et al. 2018), PSR J1544+4937 (Bhattacharyya et al. 2013). We find the center of the non-detection eclipse (excluding eclipse transitions) at an orbital phase of 0.255(5), which matches with the superior conjunction orbital phase. The estimated line-of-sight excess DM and electron column density (N_e) from timing residuals are shown in Fig. 2. The full eclipse and eclipse transition zones (shaded regions) seen in Fig. 2 can also be visualized in the schematic top view of the eclipse geometry in Fig. 1, where these regions are highlighted in dark purple and purple colors respectively. The maximum delay in timing residuals around eclipse transitions detected for PSR J1227–4853 is $888(28) \mu\text{s}$ at 591–624 MHz. This gives excess DM of $0.079(3) \text{ pc cm}^{-3}$ and N_e of $24.4(8) \times 10^{16} \text{ cm}^{-2}$ (see Fig. 2). We estimate the corresponding electron density in the eclipse region ($n_e \sim N_e/a$) as $1.5 \times 10^6 \text{ cm}^{-3}$, which is at least an order of magnitude higher than the electron density expected in the stellar wind

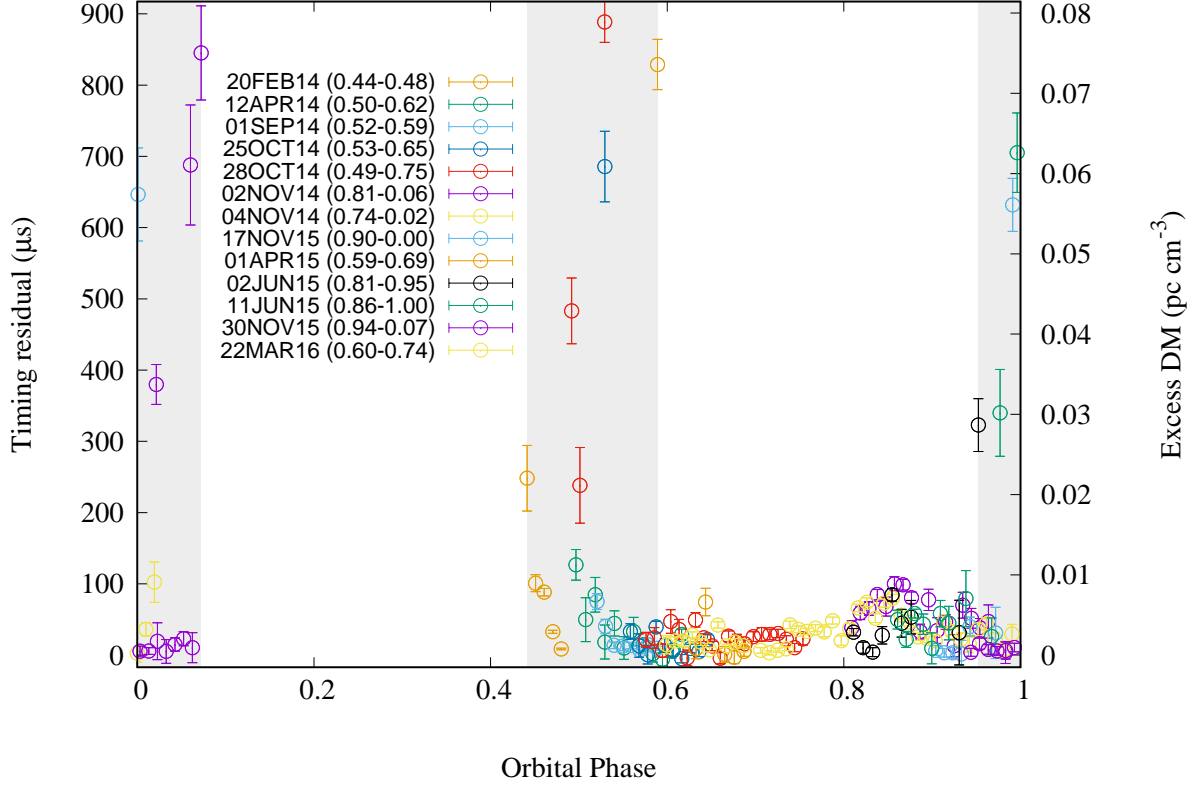


Fig. 2.— Variation of timing residual & DM with orbital phase on 13 observing epochs (denoted by different colors) at 591–624 MHz, individual epochs covering small range of full orbital phase, but collectively full orbital phase range is covered with all the observations.

(according to Johnstone et al. (2015) n_e due to the stellar wind at a distance similar to a is $\sim 10^5 \text{ cm}^{-3}$). This indicates that ablation from the companion is significantly contributing to the intra-binary material causing eclipses. This system also exhibits eclipses for a longer fraction of orbital phase. We compare the eclipse properties of PSR J1227–4853 with the known eclipsing binaries in Section 4.

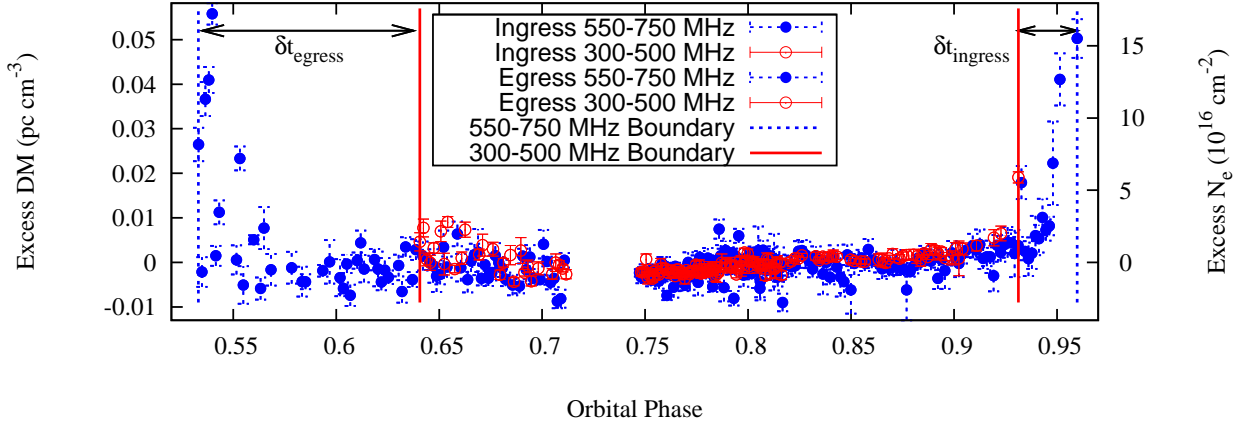


Fig. 3.— Variation of excess DM & Ne at eclipse egress & ingress boundaries measured simultaneously at 300–500 MHz (hollow red circles) & 550–750 MHz (filled blue circles). One epoch covers egress (24th May 2019) from orbital phase 0.53 to 0.82 and another covers ingress (14th May 2019) from orbital phase 0.80 to 0.96. A break seen in egress observation at orbital phase ~ 0.72 is due to re-phasing of the array.

3.2. Simultaneous dual frequency study of eclipses

In order to probe the frequency dependence of the eclipse duration for PSR J1227–4853 we carried out simultaneous dual-frequency observations at 300–500 and 550–750 MHz using the uGMRT. Observations performed on 14 May 2019 and 24 May 2019 allowed us to probe the eclipse ingress and egress transitions respectively. This eliminates the effect of temporal variations of eclipse boundaries (as seen in Fig. 2) while estimating the frequency dependence of the eclipse duration. The eclipse region for 300–500 MHz is shown by light green color in Fig. 1. Variation of the excess DM and N_e with orbital phase derived from the best-fit timing residuals are shown in Fig. 3. Eclipse boundaries are marked by vertical lines: red for 300–500 MHz and blue for 550–750 MHz. We observe a larger eclipse duration at the lower frequency band (i.e. ~ 1.2 times longer for 300–500 MHz band than 550–750 MHz band) and we note a possible asymmetry in frequency dependence of eclipse transitions in ingress and egress phase in the 300–500 MHz band compared to that in the 550–750 MHz band. The ingress starts earlier, $\delta t_{\text{ingress}} = 11.86 \pm 0.5$ minutes, and egress ends later, $\delta t_{\text{egress}} = 44.57 \pm 0.5$ minutes, at 300–500 MHz. If we consider a power-law dependence of eclipse duration with frequency ($T_{\text{eclipse}} \propto \nu^n$), we estimate a power-law index of $n = -0.44$ from these simultaneous observations. Frequency dependent eclipse durations are observed for some of the other eclipsing binaries as well. Earlier studies report that at lower frequencies the eclipse duration is seen to be larger compared to that of higher frequencies for a given

system. We have listed excess DM, pulsar wind flux (\dot{E}/a^2), eclipse duration and power-law index for eclipsing binaries in Table 1. We observed an asymmetry in eclipse boundaries between the two observing bands where $\delta t_{egress} > \delta t_{ingress}$ by 32.7 ± 0.7 minutes. From this we can derive separate power-law frequency dependence for ingress ($T_{ingress} \propto \nu^{n_i}$) and egress ($T_{egress} \propto \nu^{n_e}$) transitions (w.r.t superior conjunction), where $n_i = -0.19$ and $n_e = -0.66$.

3.3. Excess dispersion around inferior conjunction

In addition to eclipses seen at orbital phases from 0.95 up to 0.59, PSR J1227–4853 exhibits occasional occurrences of residual delays around ϕ_B of ~ 0.7 and ~ 0.8 (marked by the light purple color in the eclipse geometry in Fig. 1). This is well outside the eclipse regions, centered around inferior conjunction, $\phi_B = 0.75$ (seen in the top panel of Fig. 4). The largest excess DM and N_e we measured at $\phi_B = 0.82$ is $0.0199(6)$ pc cm $^{-3}$ and $6.1(2) \times 10^{16}$ cm $^{-2}$ respectively, which is factor of 4 lower than the values measured at the eclipse boundaries. Whereas at $\phi_B = 0.71$ we measured an excess DM of $0.0037(6)$ pc cm $^{-3}$ and N_e of $1.1(2) \times 10^{16}$ cm $^{-2}$. The durations of these phenomenon of excess dispersion measured at ϕ_B of 0.7 and 0.8 are 11.5 ± 1.7 and 27.1 ± 1.7 minutes respectively. We present three epochs of coherently de-dispersed observations at 550–750 MHz probing excess dispersion around ϕ_B of 0.82 at higher time-resolution as seen in the bottom panel of Fig. 4. The higher S/N data from the coherently de-dispersed observations allow us to probe eclipses at time resolution of 26 seconds as compared to the 591–624 MHz incoherently de-dispersed data which has time resolution of 2.3 minutes. These observations equipped with higher time-resolution and enhanced sensitivity (due to wider band-width) reveal a maximum excess DM of $0.035(3)$ pc cm $^{-3}$ and N_e of $10.8(8) \times 10^{16}$ cm $^{-2}$. We estimate the corresponding electron density in the eclipse region ($n_e \sim N_e/2a$) as 0.3×10^6 cm $^{-3}$, which is at least an order of magnitude higher than the electron density in the stellar wind (according to Johnstone et al. (2015) n_e due to stellar wind at a distance similar to separation between companion and inferior conjunction is $\sim 10^4$ cm $^{-3}$).

3.4. Continuum and pulsed flux

Aided by the capability of simultaneously recording visibilities along with the tied-array coherent beam from the GMRT interferometer, we estimated flux densities around eclipse boundaries using continuum imaging and compared that with the pulsed flux densities. Unlike pulsed flux densities the flux densities obtained from continuum imaging are expected to be unaffected by the temporal smearing caused by excess dispersion and/or scattering.

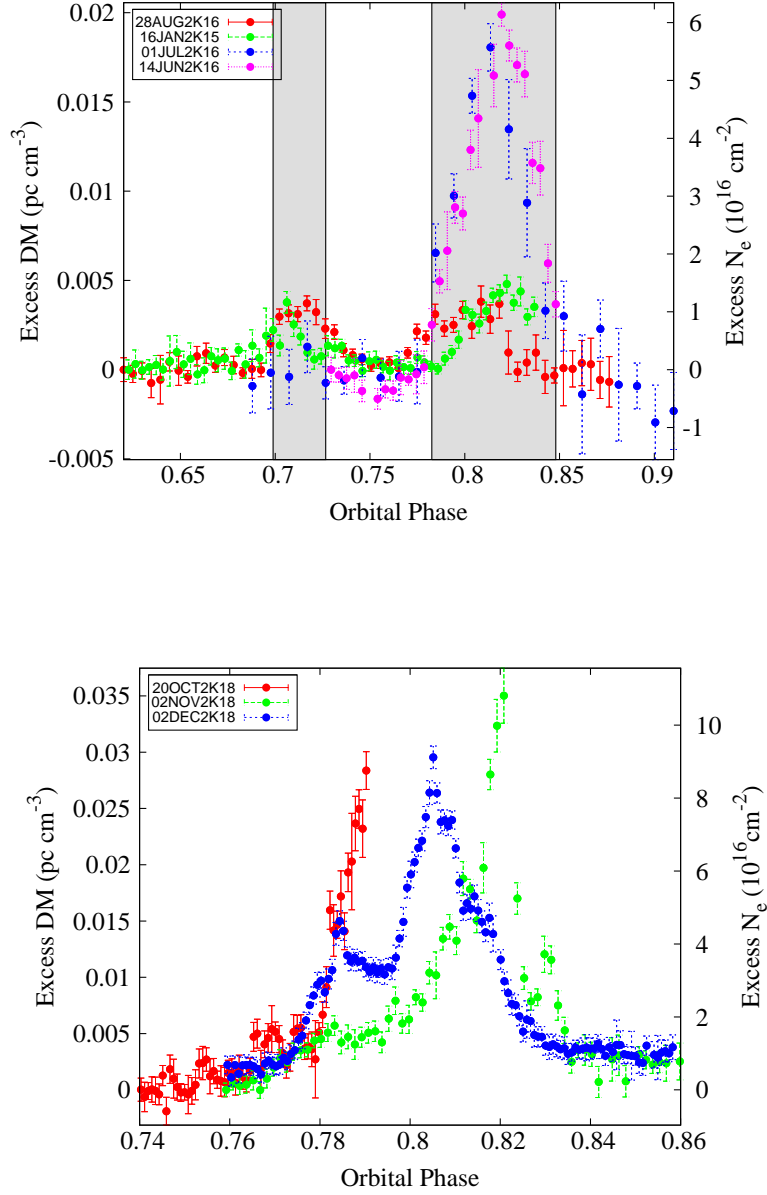


Fig. 4.— Top panel: Variation of excess DM and N_e measured around orbital phase 0.7 & 0.8 at 591–624 MHz with time resolution of 2.3 minutes. Bottom panel: Variation of excess DM and N_e measured around orbital phase 0.8 at 550–750 MHz with coherently de-dispersed observations with time resolution of 26 seconds. More sensitive data with higher time resolution brings out the pattern of variation of excess N_e with orbital phase.

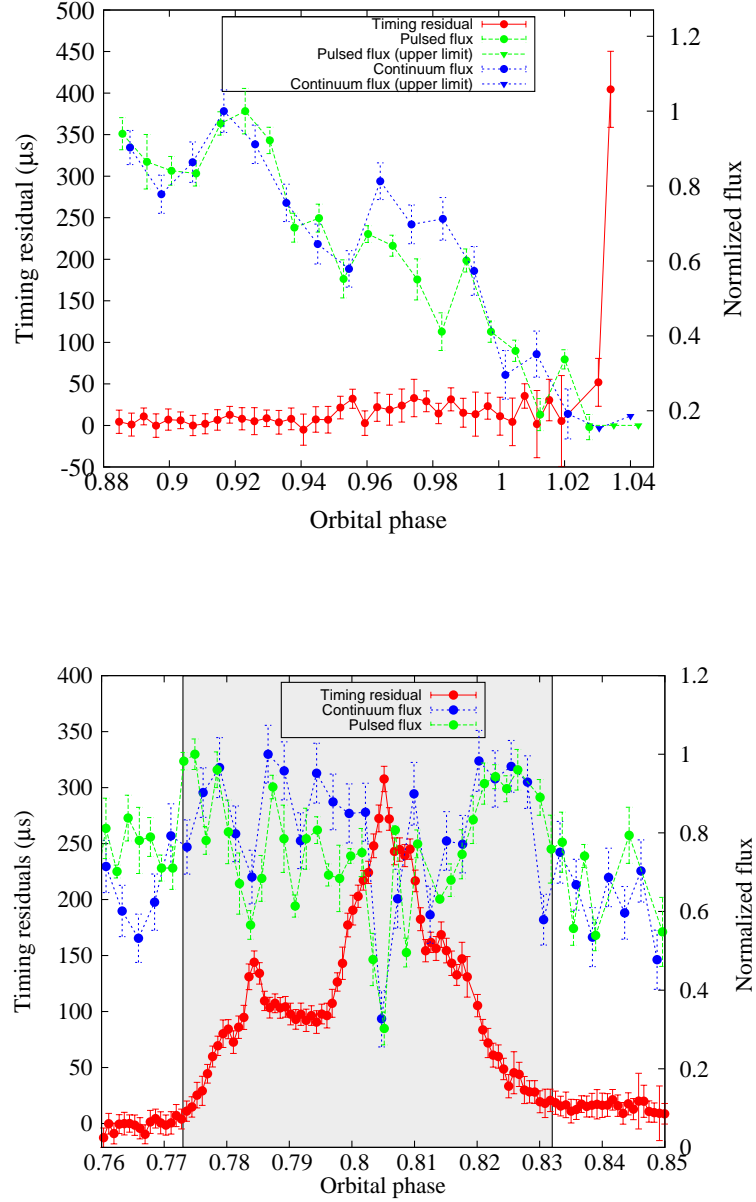


Fig. 5.— Top panel: Variation of timing residuals (added to mark start of eclipse) and flux densities (both pulsed and continuum) with orbital phase during ingress at 550–750 MHz observed on 01 Jan 2019. Bottom panel: Variation of timing residuals and continuum flux densities with orbital phase around inferior conjunction at 550–750 MHz observed on 02 Dec 2018. The highlighted region indicates the anti-correlated variation of continuum flux with timing residuals.

This comparative study of continuum and pulsed flux densities can be used for understanding the eclipse mechanism, which was done by (Roy et al. 2015) for PSR J1227–4853 while probing the egress boundary. Apart from PSR J1227–4853, imaging studies for eclipsing binaries were done by Polzin et al. (2020) for PSRs B1957+20 & J1816+4510, by Polzin et al. (2018) for PSR J1810+1744 and by Broderick et al. (2016) for PSR J2215+5135.

For PSR J1227–4853 we analyzed the imaging data (details in Section 2) to produce a lightcurve for the pulsar signal during eclipse ingress and during the instances of excess dispersion around inferior conjunction. The top panel of Fig. 5 shows the continuum (marked in blue) and pulsed (marked in green) flux densities as function of orbital phase for an eclipse ingress. A curve showing the timing residuals (marked in red) reaching up to $404 \pm 46 \mu\text{s}$ is also added in this plot. The continuum and pulsed flux densities show correlated changes as the pulsar is transitioning into eclipse at $\phi_B \sim 0.03$, where the timing residuals are rapidly increasing. We have carried out similar lightcurve analysis for the 2 Dec 2018 event of excess dispersion around $\phi_B = 0.8$. As seen in the bottom panel of Fig. 5, the TOAs (red curve) are delayed by about $307 \pm 11 \mu\text{s}$ at $\phi_B = 0.8$. The continuum flux density (blue curve) and pulsed flux density (green curve) fade in anti-correlation with the arrival times. The region with the excess dispersion delay is highlighted in bottom panel of Fig. 5. The two peaks of timing residual at $\phi_B = 0.783$ and 0.805 are exactly coinciding with two dips of the continuum and pulsed flux densities. The observed continuum flux density at $\phi_B = 0.805$ is around 30% of the peak continuum flux density measured at orbital phase $\phi_B = 0.825$. Overall the pulsed flux density is consistent with the continuum flux density. For the orbital range of 0.79 to 0.8 the pulsed flux density is a little bit lower than the continuum flux density. This could be due to the presence of temporal broadening caused by increased DM as also seen in Polzin et al. (2020). We performed light curve measurements of nearby point sources within the field-of-view showing no significant variation of flux densities over the observing span. We observed scintles of a few MHz in size, as well as flux brightening of a few minutes duration on both sides of the event of excess dispersion (orbital phase ~ 0.805), which can explain the enhancement of flux densities (highlighted region in the bottom panel of Fig. 5).

4. Discussion and Summary

We find that during ingress and egress the pulses are significantly delayed relative to best-fit timing model. The largest timing residual deviation that we measure is $888(28) \mu\text{s}$. We estimate excess DM and N_e as $0.079(3) \text{ pc cm}^{-3}$ and $24.4(8) \times 10^{16} \text{ cm}^{-2}$ respectively. The eclipse duration including ingress, egress transition for PSR J1227–4853 is about

Table 1: Parameters for eclipsing binary millisecond pulsar systems listed in column 1 indicating its type, redback (RB) or black widow (BW). Column 2 presents the excess dispersion. Column 3 presents \dot{E}/a^2 where \dot{E} is spin-down energy of the pulsar and a is distance to the companion. Column 4 presents eclipse duration with corresponding frequency in parenthesis. Column 5 denotes the index of power-law dependence (n) of full eclipse duration with frequency.

Pulsar Name	Excess DM (pc cm ⁻³)	$\dot{E}/a^{2\alpha}$ (10 ³⁵) (erg/s/ R_{\odot}^2)	Eclipse duration ^{β}	n	Reference ^{ζ}
J1023+0038 (RB)	0.15(700)	0.33	40(685)	-0.41	1
J1048+2339 (RB)	0.008(327)	0.03	57(327)	–	10
J1227–4853(RB)	0.079(607)	0.29	64(607)	-0.44	2
J1227–4853 ^{γ} (RB)	0.035(607)	–	6(607)	–	2
J1544+4937 (BW)	0.027(607)	0.11	13(322)	–	3
J1723–2837 (RB)	–	0.04	26(1520)	–	4
B1744–24A (RB)	0.6(1499.2)	–	$\sim 50^{\delta}$ (820)	–	5
J1810+1744 (BW)	0.015(325)	0.18	13(149)	-0.41	6
J1816+4510 (RB)	0.01(149)	0.08	24(121)	-0.49 ^{ϵ}	8
B1957+20 (BW)	0.01(149)	0.22	18(121)	-0.18	8
J2051–0827 (BW)	0.13(705-4023)	0.06	28(149)	-0.41	7,8
J2215+5135 (RB)	–	0.28	66(149)	-0.21 ^{ϵ}	8,9

α : Using <https://apatruno.wordpress.com/about/millisecond-pulsar-catalogue/>

β : The eclipse duration (in % of orbit) includes non-detection and associated ingress, egress transition.

γ : Parameters for excess dispersion observed around inferior conjunction.

δ : For majority of the observed eclipses. However, observed eclipse durations are variable and sometimes completely enshrouding the pulsar (Bilous et al. 2019).

ϵ : The value of the estimated power law index using all available frequency measurements as given in the recent literature.

ζ : List of references; 1: Archibald et al. (2009); 2: Current work; 3: Bhattacharyya et al. (2013); 4: Crawford et al. (2013); 5: Bilous et al. (2019); 6: Polzin et al. (2018); 7: Polzin et al. (2019); 8: Polzin et al. (2020); 9: Broderick et al. (2016), 10: Deneva et al. (2016)

265 \pm 3 minutes (64% of its orbit), indicating that for a larger fraction of its orbit the pulsar is enshrouded by the intra-binary materials. From Table 1 we note that the observed values of excess DM, N_e , eclipse duration and \dot{E}/a^2 for PSR J1227–4853 are similar to PSR J1023+0038, which is the other LMXB–MSP transitioning system. An asymmetry

is seen between egress and ingress duration, egress being longer by 12.4 ± 3 minutes. This asymmetry can be caused by a tail of eclipsing material swept back due to orbital motion of companion, which is also observed for other eclipsing binaries (e.g. Polzin et al. (2020)). Such asymmetries can be generated by the interaction of out-flowing gas from companion with pulsar radiation, which can create increased density in the trailing part of the outflow as shown using hydrodynamical simulation by Tavani et al. (1991) suggesting this as the explanation for the observed eclipses of PSR B1957+20 (Fruchter et al. 1990). From the dual frequency observations on two epochs one covering egress boundary and another covering ingress boundary, we observed that 300–500 MHz eclipse duration is longer than 550–750 MHz. A longer eclipse duration at lower frequencies is also observed for other eclipsing binaries (Broderick et al. (2016), Polzin et al. (2018), Stappers et al. (2001), Polzin et al. (2020)). In addition we observe that for PSR J1227–4853 ingress boundary starts earlier (~ 11.9 minutes) and egress ends later (~ 44.6 minutes) at lower frequency (300–500 MHz) than at higher frequency (550–750 MHz), i.e. $\delta t_{egress} > \delta t_{ingress}$ by 32.7 ± 0.7 minutes.

We estimate the power law index for the frequency dependent eclipse duration as $n = -0.44$. From Table 1, we find generally redback pulsars have relatively longer eclipse duration and excess DM at the eclipse boundaries compared to the black widow systems. Future study of a statistically significant sample of such eclipsing binaries over a wide frequency range is warranted for better understanding.

We observe a fading of the pulsar flux density around inferior conjunction ($\phi_B \sim 0.7$ & 0.8) which is also associated with an excess timing delay on several occasions ($\sim 25\%$ of all observations). To our knowledge such systematic change of flux density around a fixed orbital phase (i.e. inferior conjunction in this case) is not reported for any other eclipsing binary. Occasional clustering of fragmented blobs of plasma around the inferior conjunction could possibly lead to such decrease in flux. The maximum value of excess DM and N_e observed around inferior conjunction ($\phi_B = 0.82$) is factor of two to four times lower than that observed at the eclipse boundary for PSR J1227–4853. In this context we note that for PSR J1544+4937 (having very similar excess DM and N_e as seen in PSR J1227–4853) frequency dependent eclipsing around superior conjunction is observed, where the pulsed signal exhibits a decrease in flux at higher frequency (~ 607 MHz) and is completely eclipsed at lower frequency (~ 322 MHz) as reported by Bhattacharyya et al. (2013). Future investigations of PSR J1227–4853 at lower frequencies may reveal frequency dependent eclipsing around inferior conjunction. Short eclipses are generally seen around eclipse region centered on superior conjunction in other eclipsing binaries, e.g. for PSR J1544+4937 by Bhattacharyya et al. (2013). However for PSR J1227–4853 we observe the phenomenon of excess dispersion with flux fading preferentially centered around inferior conjunction. According to de Martino et al. (2015), the X-ray emission originates in an intra-binary shock produced by the interaction

of the outflow from the companion and the pulsar wind. We also note that de Martino et al. (2015) observed a dip in the count rate centered at $\phi_B = 0.75$ while monitoring X-ray orbital modulation of the pulsar. Radio observations reported in this paper have at least an order of magnitude better orbital phase resolution than the X-ray observations, which possibly allowed us to resolve the single dip seen in X-ray in two symmetric dips observed in radio around inferior conjunction. Tavani et al. (1991) explained the observed eclipse properties for PSRs B1957+20 and B1744–24A using hydrodynamical simulations of the companion’s wind outflow. They showed that the eclipses are created due to the shocks generated by interaction between the pulsar radiation and the out flowing gas from the companion star. They explained drastic eclipse changes observed for PSR B1744–24A by Lyne et al. (1990), while inferring that the eclipse shape is dependent on the thermal and kinetic state of the out flowing gas which could be time variable. By progressively decreasing mass loss rate Tavani et al. (1993) arrived at a final mass configuration allowing the pulsar to be visible for a large fraction of orbital phase. Whereas for progressively increasing or for a constant but relatively large value of the mass loss rate, pulsar could get completely enshrouded. According to Linial et al. (2017) mass transfer through L2 Lagrangian point could happen for a system having rapid orbital evolution. In case of PSR J1227–4852 mass transfer during accretion phase through L2 could be responsible for material floating around inferior conjunction causing excess dispersion. The observed occasional flux fading around the inferior conjunction for J1227–4853 could also be caused by systematic changes in final mass configurations achieved via variations in the mass loss rate or other parameters such as temperature or Mach number. Frequent multi-frequency observations are planned to probe this in more detail.

From simultaneous timing and imaging analysis we find pulsed and continuum flux densities of PSR J1227–4853 follow a similar trend at eclipse ingress. Roy et al. (2015) reported similar finding at eclipse egress for the same pulsar. In earlier studies the decrease of continuum flux densities at eclipse boundaries were reported by Polzin et al. (2018) for PSR J1810+1744 and by Broderick et al. (2016) for PSR J2215+5135. We also measure the variations of continuum flux densities around inferior conjunction (presented in Section 3.3) and find that minima in continuum flux density coincides with the maxima in excess dispersion.

Now we investigate possible eclipse mechanisms following Thompson et al. (1994). In order to study the pulse smearing due to dispersion as a cause of the eclipse, $DM \sim 1.3 \text{ pc cm}^{-3}$ is required to disperse pulsed emission completely. However, the measured largest excess DM at eclipse boundary is $0.079(3) \text{ pc cm}^{-3}$ which is a factor of ~ 16 less and hence rule out the dispersion as the cause of eclipse. The scattering due to excess N_e can broaden the pulse and change pulse profile. However, we have not seen any signature of profile evolution at

eclipsing boundaries. Thus scattering as a cause is ruled out. Moreover, temporal smearing due to the dispersion or scattering is not expected to change the continuum flux density. For refraction to be the cause of the eclipse the expected group delay at the ingress or egress would be $\sim 10\text{--}100$ ms as reported by Thompson et al. (1994). We measure maximum time delay around eclipse boundary $\sim 888 \mu\text{s}$, for PSR J1227–4853, which is at least an order of magnitude smaller than the group delay required for refraction of radio beam causing eclipse. This implies refraction can not be the cause of eclipse. For an eclipsing binary system with temperature T and clumping factor of the eclipsing medium f_{cl} ($f_{cl} = \langle n_e^2 \rangle / \langle n_e \rangle^2$), the optical depth due to free-free absorption is given by Equation 1 (Thompson et al. 1994), where N_e is electron column density, L is absorption length.

$$\tau_{ff} \simeq 3.1 * 10^{-8} \frac{f_{cl}}{T_7^{3/2}} N_{e,17}^2 L_{11}^{-1} \quad (1)$$

Using Equation 1 we derive, $T \leq 10^2 \times f_{cl}^{2/3}$ K, as relation between the temperature T and clumping factor of the eclipsing medium. This indicates that for free-free absorption to be the cause of eclipse (i.e. $\tau_{ff} > 1$) in PSR J1227–4853 with $N_e = 24.4 \times 10^{16} \text{ cm}^{-2}$ at eclipse boundary and absorption length about twice the size of the eclipse zone, we need either very high clumping factor or very low temperature. Assuming a temperature range from an unheated star to an irradiated star (i.e. $5500 - 500000$ K) according to de Martino et al. (2014), we expect the range of clumping factor to be 400 to 3.5×10^5 , which is not physically possible (Muijres 2012), ruling out free-free absorption as the cause of eclipse. Considering PSR J1227–4853 has an average flux density at 650 MHz (S_ν^0) ~ 1.2 mJy, spectral index (α) ≥ -1.8 and distance (d_{kpc}) ~ 1.4 kpc, demagnification (M) $\sim (R_c/2r)^2$, where R_c is radius of curvature of plasma cloud and r is distance from center of curvature, the induced Compton optical depth can be calculated with Equation 2 (Thompson et al. 1994).

$$\tau_{ind} \simeq 4 * 10^{-5} \frac{N_{e,17}^2 S_\nu^0}{\nu_9^2} |\alpha + 1| \left(\frac{d_{kpc}}{a_{11}} \right)^2 M \quad (2)$$

We calculate the upper limit of induced Compton depth $\tau_{ind} \leq 7.6 \times 10^{-5}$, which rules out induced Compton scattering to be the cause of the eclipse. The decrease of continuum flux density at eclipse boundary as well as flux fading around inferior conjunction indicates absorption of pulsar flux by line-of-sight material could be a plausible cause of eclipse. In order to check if cyclotron-synchrotron absorption of pulsar emission by non-relativistic or relativistic electrons is the cause of the eclipse we estimate the magnetic field of the eclipsing plasma with Equation 3 (Thompson et al. 1994) where $m = \nu/\nu_B$, $\omega_B = 2\pi\nu_B = eB/m_e c$.

$$B = 350 m^{-1} \nu_9 \text{ G} \quad (3)$$

We calculate the magnetic field in the vicinity of the companion to be 27G, and the cyclotron fundamental frequency to be 77 MHz. Observed eclipses reported in this paper for PSR J1227–4853 are centered at 322 & 607 MHz which are 4th and 8th harmonics of this cyclotron fundamental frequency. In this context, we note that eclipses for PSR J1544+4937 have been seen up to 20th harmonic of its fundamental cyclotron frequency (Bhattacharyya et al. 2013). For PSR J1227–4853 cyclotron absorption at fundamental cyclotron frequency and its lower harmonics can be the cause of eclipse. The observed larger frequency dependence of the eclipse egress compared to the ingress can also be explained by the the presence of more stellar material around the eclipse egress than ingress which could result into enhanced frequency dependence of cyclotron absorption optical depth. Since cyclotron absorption optical depth decreases for higher harmonics, it will be useful to probe the eclipse phase for this pulsar at higher frequencies. We plan to estimate the companion’s magnetic field near the eclipse boundaries via studying the variation of rotation measure values (Polzin et al. 2019; Li et al. 2019).

To summarize, in this paper we report a detailed multi-frequency study of the eclipse properties for PSR J1227–4853. In addition to regular eclipses around superior conjunction, the system also shows evidence of excess dispersion and flux fading around inferior conjunction. Simultaneous studies of pulsed and continuum flux densities indicate flux removal possibly due to the cyclotron absorption rather than temporal smearing as the cause of eclipse, both for regular eclipse as well as for flux fading at inferior conjunction.

We acknowledge support of the Department of Atomic Energy, Government of India, under project no. 12-R&D-TFR-5.02-0700. The GMRT is run by the National Centre for Radio Astrophysics of the Tata Institute of Fundamental Research, India. We acknowledge support of GMRT telescope operators for observations. We acknowledge discussions with Devojoyoti Kanasabanik. BWS acknowledges funding from the European Research Council (ERC) under the European Unions Horizon 2020 research and innovation programme (grant agreement No. 694745)

REFERENCES

- Archibald, A. M., Stairs, I. H., Ransom, S. M., et al., 2009, *Science*, 324, 1411.
- Bhattacharyya, B., Roy, J., Ray, P. S., et al., 2013, *ApJ Letters*, 773, 12.
- Bhattacharya, D., 1992, *NATO Advanced Research Workshop on X-Ray Binaries and the Formation of Binary and Millisecond Radio Pulsars*, p. 257.
- Bilous, A. V., Ransom, S. M., Demorest, P., 2019, *The Astrophysical Journal*, 877, 125.

- Broderick, J. W., Fender, R. P., Breton, R. P., 2016, MNRAS 459, 2681.
- Chengalur, J. N., 2013, Technical Report NCRA/COM/001.
- Crawford, F., Lyne, A. G., Stairs, I. H., et al., 2013, The Astrophysical Journal, 776, 20.
- de Martino, D., Casares, J., Mason, E., et al., 2014, MNRAS 444, 3004.
- de Martino, D., Papitto, A., Belloni, T., et al., 2015, MNRAS 454, 2190.
- Deneva, J. S., Ray, P. S., Camilo, F., et al., 2016, ApJ, 823, 105.
- Eggleton P. P., 1983, ApJ, 268, 368.
- Fruchter, A. S., Berman, G., Bower, G., et al., 1990, ApJ, 351, 642.
- Fruchter, A. S., Gunn, J. E., Djorgovski, S. G., et al., 1988, IAU Circ., No. 4617, #1.
- Johnstone C. P., Güdel, M., Lüftinger, T., et al., 2015, A&A, 577, 22.
- Li, D., Lin, F., Main, R., 2019, MNRAS, 484, 5723.
- Itai Linial, Re'em Saree, 2017, MNRAS, 469, 2441.
- Lyne, A. G., Manchester, R. N., D'Amico, N., et al., 1990, Nature, 347, 650.
- Main, R., Yang, I-Sheng, Chan, V., et al., 2018, Nature, 557, 522.
- Mohan, N., Rafferty, D., 2015, Astrophysics Source Code Library, 2015ascl.soft02007M.
- Muijres L. E., Vlink, J. S., de Koter, A., et al., 2012, A&A 526, A32.
- Nice, D. J., Thorsett, S. E., 1992, ApJ, 397, 249.
- Polzin, E. J., Breton, R. P., Clarke, A. O., 2018, MNRAS 476, 1968.
- Polzin, E. J., Breton, R. P., Stappers, B. W., et al., 2019, MNRAS, 490, 889.
- Polzin, E. J., Breton, R. P., Bhattacharyya, B., et al., 2020, MNRAS, 494, 2948.
- Roy, J., Gupta, Y., Ue-Li Pen et al., 2010, Experimental Astronomy, 28, 25.
- Roy, J., Ray, P. S., Bhattacharyya, B., Stappers, B., et al., 2015, ApJ Letters, 800, 12.
- Ryba, M. F., Taylor, J. H., 1991, ApJ, 371, 739.
- Ransom, S. M., Eikenberry, S. S., Middleditch, J., 2002, AJ, 124, 1788.

Stappers, B. W., Bails, M., Lyne, A. G., et al., 1996, *ApJ*, 465, 119.

Stappers, B. W., Bailes, M., Lyne, A. G., et al., 2001, *MNRAS*, 321, 576.

Tavani, M., Brookshaw, L., 1991, *ApJ*, 381, 21.

Tavani, M., Brookshaw, L., 1993, *A&A*, 267, 1.

Thompson, C., Blandford, R. D., Evans, C. R., et al., 1994, *ApJ*, 422, 304.